Optica Applicata, Vol. LV, No. 4, 2025
DOI: 10.37190/oa/213501

Generation of spatial transverse optical vortices via 4π tight focusing radially polarized light

Kailing Yao[1], Yuhao Zhang[1], Yu Miao[1], Lingyu Wang[1], Kadier Ayikanbaier[2], Mengru Zhao[1], Huizhe Li[1], Xiumin Gao[1,*], Xiaoyu Weng[2], Songlin Zhuang[1]

[1] University of Shanghai for Science and Technology, 516 Jungong Road, Shanghai 200093, China

[2] College of Physics and Optoelectronic Engineering, Key Laboratory of Optoelectronic Devices and Systems of Ministry of Education and Guangdong Province, Shenzhen University, Shenzhen 518060, China

[*] Corresponding author: gxm@usst.edu.cn

Spatial transverse optical vortices (STOVs), characterized by possessing transverse orbital angular momentum, offer new degrees of freedom for optical manipulation. However, since the vortex phase circulation of STOVs is the spatiotemporal plane (*x*-*t* plane), traditional phase modulation methods based on the *x*-*y* transverse plane are no longer applicable. Therefore, exploring new methods for generating STOVs has become a significant challenge. Here, a 4π tight focusing system with overlapped phase from two counter-propagating radially polarized beams is proposed to generate STOVs. First, by independently designing the phase wavefronts of counter-propagating beams, uniform nano-scale spherical spots are generated in the focal region. Then, treating spherical spots as spatial trajectory units and superimposing a time-dependent helical phase factor $\exp(-il\varphi_{st})$, precise control over the spot's spatial position and motion trajectory is achieved. When the temporal step is sufficiently small, *i.e.*, under high temporal resolution, smooth STOVs emerge. Through simultaneous modulation of temporal and spatial factor, STOVs with distinct radii *r* can be generated. This approach ultimately enables precise customization of STOVs in size, smoothness, and geometry, facilitating high-precision advancements in fields such as super-resolution microscopy, quantum manipulation and subwavelength nonlinear optical effects.

Keywords: spatial transverse optical vortices, orbital angular momentum, 4π tight focusing, spherical spots.

1. Introduction

Optical vortices (OVs), as particular electromagnetic structures that carry a spatially rotated flow of energy density around a phase singularity, have attracted significant attention in the fields of optics and photonics in recent years. Typically, OVs with flow of energy density along the propagation direction carry longitudinal orbital angular momentum (OAM). OAM is generated by applying a helically increasing (or decreasing)

phase factor $\exp(-il\varphi)$ in the transverse plane, where φ is the azimuthal angle, and l is an integer referred to as the topological charge. With such a degree of freedom, longitudinal OAM enables various advanced applications in optical imaging [1-3], optical communication [4-6], quantum key distribution [7-10], and optical trapping [11-13].

In the tightly focused spatiotemporal domain, OVs with flow of energy density perpendicular to the propagation direction, known as spatial transverse optical vortices (STOVs), have been reported [14-19]. Since the transverse OAM of STOVs is perpendicular to the axial direction, with the transverse plane being the *x*-*z* plane, conventional methods for generating OVs through modulation in the *x*-*y* plane are no longer applicable. Currently, researchers have demonstrated the generation of STOVs using a 4*f* pulse shaper, and combined it with a spatial light modulator to control the spectral phase [20,21], successfully producing a series of STOVs with multiple OAM modes and dozens of STOVs within a single pulse [14]. Additionally, some researchers have proposed an optical spatial-temporal differentiator to generate STOVs, where the interference of the produced STOVs can be used to detect sudden changes in the envelope of spatial and temporal pulse shapes [22]. Building upon these advancements, we present a novel approach for generating STOVs. This method integrates the fundamental principles of spectral phase modulation and spatial beam shaping, while featuring a substantially simplified optical architecture. Such improvements enhance the control flexibility of STOVs field generation and manipulation, offering promising prospects for further research.

In this paper, we theoretically demonstrate a novel method to generate spatially varying uniform STOVs by 4π tight focusing system. By independently designing the phase wavefronts of counter-propagating beams, we generate a uniform nano-scale spherical spots in the focal region. Then, treating spherical spots as spatial trajectory units and superimposing a time-dependent helical phase factor $\exp(-il\varphi_{st})$ allows for precise control over both the spatial position and movement trajectory of the light spots. This enables the generation of arbitrary dispersion patterns and trajectory manipulations in the spatio-temporal domain. When the temporal step is sufficiently small, *i.e.*, under high temporal resolution, smooth STOVs emerge. Through simultaneous modulation of temporal and spatial factor, STOVs with distinct radii r can be generated. This approach ultimately enables precise customization of STOVs in size, smoothness, and geometry, facilitating high-precision advancements in fields such as super-resolution microscopy, quantum manipulation, and subwavelength nonlinear optical effects.

2. Methods

Figure 1 illustrates the 4π tight focusing system composed of two high numerical aperture (NA) objectives positioned left and right, each illuminated by counter-propagating RP beams. Short arrows denote the instantaneous electric field vectors. The two counter-propagating RP beams are focused by the left and right objectives, resulting in overlapping foci at the system's focal plane.

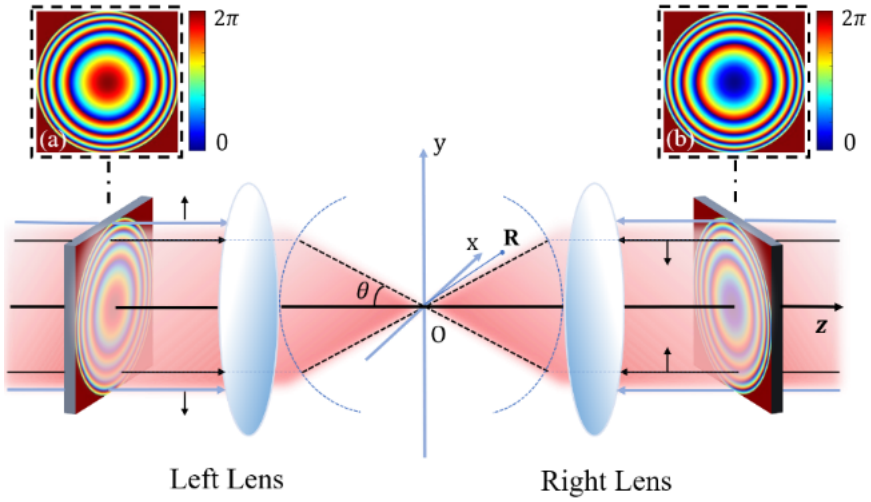

Fig. 1. Schematic of a 4π tight focusing system illuminated by two counterpropagating radially polarized (RP) beams. The phase modulation patterns applied to the (a) left and (b) right objective lenses.

When the polarization directions of the incident light fields on either side of the 4π tight focusing system are opposite and a phase difference of π is introduced between them, the radial components of the electric field near the focus interfere destructively. Moreover, when the incident angle θ is small, the longitudinal component of the electric field near the focus is negligible. However, as θ increases, the longitudinal electric field component gradually strengthens. Consequently, when θ becomes sufficiently large, the light intensity near the focus no longer vanishes, leading to the formation of a focused spot. According to Richards and Wolf's classical vector diffraction theory, after a light beam is focused by a single high numerical aperture lens, the electric field distribution at the focal plane is [23,24]:

$$\mathbf{E}(r,\varphi,z) = \frac{-ik}{2\pi}\int_0^{\alpha} \mathrm{d}\theta \int_0^{2\pi} \mathbf{E}(\theta,\phi)\sin\theta\exp(il\varphi_{\mathrm{st}})\exp(ik\,\mathbf{s}\cdot\mathbf{r})\mathrm{d}\phi \tag{1}$$

where k is the wave number in free space, given by $k = 2\pi/\lambda$, where λ is the corresponding incident wavelength; α denotes the maximum value of the convergence angle, where $\alpha = \arcsin(\mathrm{NA}/n_0)$ and NA is the numerical aperture, and n_0 is the refractive index in the image space; $l\varphi_{\mathrm{st}}$ denotes the spatiotemporal spiral phase and $\varphi_{\mathrm{st}} = \tan^{-1}(x/t)$; $\mathbf{s}$ is the direction of light propagation through the objective lens. The field strength factor $\mathbf{E}(\theta,\phi)$ is:

$$\mathbf{E}(\theta,\phi) = \mathrm{circ}\left(\frac{\sin\theta}{\sin\alpha}\right) P(\theta)\,l(\theta)(\cos\phi_0\,\mathbf{e}_{\mathrm{r}} + \sin\phi_0\,\mathbf{e}_{\phi}) \tag{2}$$

For an observational point R in the vicinity of the focus, we have

$$\mathbf{s}\cdot\mathbf{r} = z\cos\theta + r\sin\theta\cos(\phi-\theta) \tag{3}$$

The three-dimensional electric field distribution in the focal area of the high-resolution aperture objective lens in the cylindrical coordinate system is:

$$\mathbf{E}_{\mathrm{r}}(r, \varphi, z) = A\int_0^{\alpha} \sin 2\theta P(\theta) l(\theta) J_1(kr\sin\theta)\exp(il\varphi_{\mathrm{st}})\exp(ikz\cos\theta)\,\mathrm{d}\theta \tag{4}$$

$$\mathbf{E}_{\mathrm{z}}(r, \varphi, z) = 2iA\int_0^{\alpha} \sin^2\theta P(\theta) l(\theta) J_0(kr\sin\theta)\exp(il\varphi_{\mathrm{st}})\exp(ikz\cos\theta)\,\mathrm{d}\theta \tag{5}$$

where $\mathbf{E}_{\mathrm{r}}(r, \varphi, z)$ and $\mathbf{E}_{\mathrm{z}}(r, \varphi, z)$ represent the longitudinal and radial electric field components, respectively, at the observation point R near the focus. Here, $P(\theta)$ is the pupil function. For an equidistant lens, $P(\theta) = \cos^{1/2}\theta$, while for a Herschel lens, $P(\theta) = 1$. In this case, we choose to use a Herschel lens. A represents the amplitude constant. $J_{\mathrm{n}}(x)$ represents the Bessel function of the first kind of order n. $l(\theta)$ represents the electric field of the incident light beam. The Laguerre–Gaussian (LG) beam is a special case of a vortex beam, and the expression for the LG beam used in the simulation is as follows:

$$l_0(\theta) = \left(\frac{f\sin\theta}{w}\right)^m \exp\left[-2\left(\frac{f\sin\theta}{w}\right)^2\right] \tag{6}$$

where w is the beam waist, f is the focal length of the high numerical aperture lens, and m is the topological charge, with $m = 1$, $w = 0.01$ m, and $f = 0.01$ m.

By determining $l(\theta)$ to correspond to the generation of the same spherical light spot when translated along the optical axis to another position $z = z_0$. $l(\theta)$ can be expressed as follows:

$$l(\theta) = l_0(\theta) A(\theta) \tag{7}$$

with,

$$A(\theta) = \sum_{n=0}^{\infty} \frac{i^{-n}}{2}(-1)^n(2n+1) j_n(kz_0) P_n(\cos\theta) \tag{8}$$

Here, $A(\theta)$ is determined by the spherical wave expansion of the plane wave factor from the Richards–Wolf integral. $P_n(x)$ denotes the Legendre polynomial of order n. We aim to generate the same spherical light spot when translating to another position $x = x_0$, where x can be derived from the transformation between Cartesian and spherical coordinates.

The selection of the NA of the objective ensures that the maximum convergence angle from the edge of the lens is 89°, preventing $l(\theta)$ from becoming infinite and facilitating the generation of the largest possible gradient force. In order to achieve perfect destructive interference of the transverse components in the focal plane while

increasing the electric field strength, two counter-propagating RP beams must have opposite polarization directions. This minimizes the scattering force and maximizes the gradient force. Based to the structure of the 4π tight focusing system, the electric field expression near the focus is given by:

$$E(r, \varphi, z) = E_1(r, \varphi, z) + E_2(-r, \varphi, -z) \tag{9}$$

where E_1 and E_2 represent the electric fields generated by the left and right lenses, respectively. The negative sign of r in E_2 indicates the opposite polarization direction of the two incident beams, while the negative sign in z reflects the counter-propagating direction of the beams.

By precisely controlling the amplitude, polarization, and phase distribution of spherical light spots, subwavelength-scale super-diffraction-limited light field control can be achieved in three-dimensional space. Within this framework, the highly localized spherical light spots generated can be regarded as the basic spatial units in optical control, *i.e.*, "optical pixels". Each light pixel not only possesses nanoscale spatial positioning capability but can also be endowed with rich intrinsic structural features through the introduction of specific spatio-temporal phase modulation.

By applying appropriate spiral phase modulation to two incident light fields, the electric field distribution at the focal point can form a topological structure with phase singularities and orbital angular momentum. At this point, the originally symmetric spherical light spot evolves into a novel non-propagating localized light field—the spatiotemporal optical vortex.

3. Results

This section investigates the spatially transverse OVs generated by tight focusing radially polarized light using a 4π system. Numerical integration of Eq. (7) is performed with parameters $\lambda = 1$ and NA = 0.95. For simplicity, we assume a refractive index $n = 1$ and an amplitude constant $A = 1$. Wavelength λ is used as coordinate unit in all figures.

In a single-lens system, the longitudinal dimension of the radially polarized beam is larger than its transverse dimension, primarily due to the greater extent of light propagation along the optical axis, resulting in a relative increase in longitudinal size. In contrast, in a 4π tight focusing system, the two counter-propagating beams converge at the same point, leading to interference of the wavefronts at the focus. This interference effect significantly reduces the longitudinal size of the focus, creating a more compact focusing region near the focal point. Figure 2 illustrates the total intensity distribution in the *z*-*x* plane at a wavelength of 532 nm for both the 4π and the 2π focusing system. Figure 2(a) shows the 3D iso-intensity ($I = I_{\max}/2$) surface distribution in the focus region after being focused by a 4π tight focusing system. Figures 2(b) and (d) show the total intensity distribution and the radial and axial intensity profiles in the *z*-*x* plane for the 4π system, while Figs. 2(c) and (e) display the corresponding distributions for the 2π system. The peak intensity for each mode is normalized to 1. Comparing Figs. 2(b) and (d) with (c) and (e) reveals that the radial dimensions are both 0.4λ, while

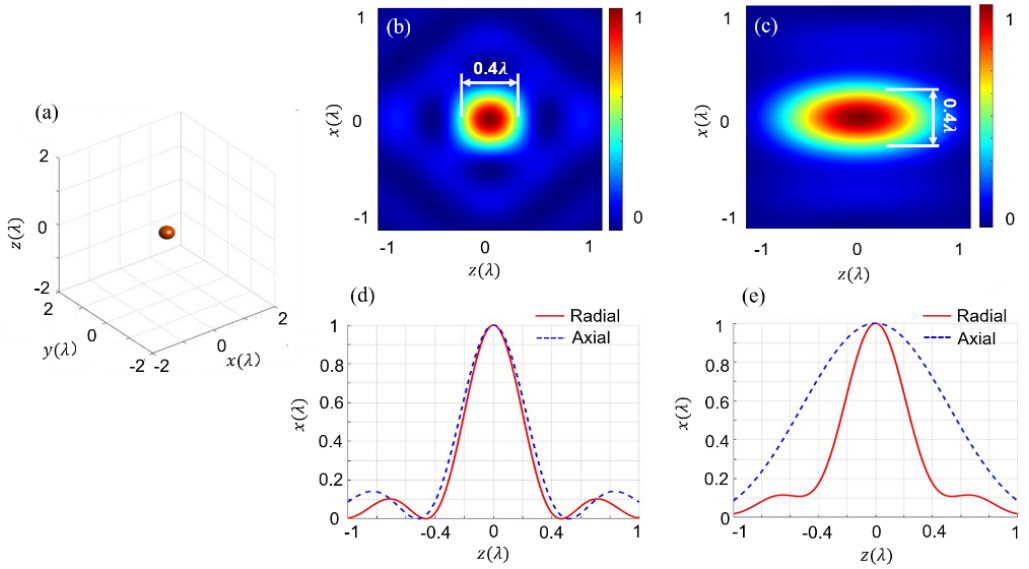

Fig. 2. Comparison of single quasi-spherical focal point produced by 4π and 2π tight focusing systems. (a) 3D iso-intensity ($I = I_{max}/2$) surface distribution in the focus region. (b) and (c) Total intensity distributions in the *z*-*x* plane at a wavelength of 532 nm for the 4π and 2π focusing systems. (d) and (e) Normalized intensity distributions near the focal points of 4π and 2π systems.

the axial dimensions of the 4π tight focusing system are 0.4λ, and the axial dimensions of the 2π focusing system are 1.2λ. The focal point with the full width half maximum (FWHM) of the focal spot which generated by 4π tight focusing system along the *x*-, *y*-, and *z*-axis are $\Delta x = 0.4\lambda$, $\Delta y = 0.4\lambda$, and $\Delta z = 0.4\lambda$, respectively. Their central 2D spot area was calculated as $S\text{-}xy = 0.16\lambda^2$, $S\text{-}yz = 0.16\lambda^2$ and $S\text{-}zx = 0.16\lambda^2$, respectively. The volume of the sphere is $0.064\lambda^3$. This shows that the light spot focused by the 4π tight focusing system effectively reduces the axial size of the focal point, resulting in a tighter and sharper spot. This is primarily due to the perfect destructive interference between the two counter-propagating beams, which diminishes the total radial component within the focal plane to zero, thereby significantly reducing the size of the light spot.

In order to precisely control the position of the spherical spot to ensure that it moves in three-dimensional space, our study changes the input field by changing the phase. The input field $l(\theta)$ can be obtained from the fundamental radially polarized mode through dual-band phase modulation, which can be implemented using a spatial light modulator. Figures 3(a)–(e) illustrate the intensity distribution near the focus for different values of x_0, and show the evolution of the intensity of the spherical light spot as the parameter x_0 continuously varies from -2λ to 2λ, specifically for $x_0 = -2\lambda$, -1λ, 0, 1λ, 2λ. As x_0 changes, the central focus gradually moves along the *x*-axis. When $x_0 = 0$, the spot is precisely located at $x = 0$, and as x_0 increases, the central focus moves

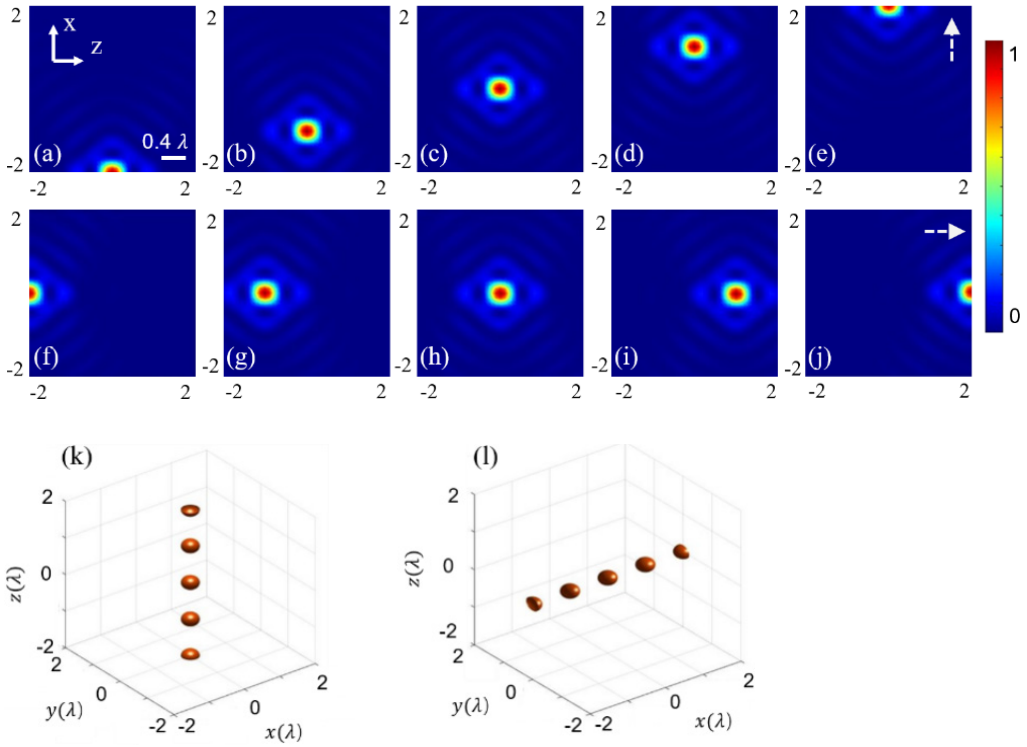

Fig. 3. Evolution of the intensity of spherical light spot near the focus. (a)–(e) Spherical light spots obtained at $x_0 = -2\lambda, -1\lambda, 0, 1\lambda, 2\lambda$, respectively. (f)–(j) Spherical light spots obtained at $z_0 = -2\lambda, -1\lambda, 0, 1\lambda, 2\lambda$, respectively. (k) and (l) The distribution of a spherical spot in the focal area along the z-axis and along the x-axis of a 3D surface of equal intensity.

away from the center and gradually shifts upward, maintaining perfect spherical symmetry in the focused beam. Phase modulation only changes the position of the spherical light spot and does not affect the intensity distribution and polarization distribution of the light spot.

Figures 3(f)–(j) display the intensity distribution near the focus for different values of z_0, and represent the evolution of the intensity of the spherical light spot as the parameter z_0 continuously varies from -2λ to 2λ, specifically for $z_0 = -2\lambda, -1\lambda, 0, 1\lambda, 2\lambda$. As anticipated, we obtain a series of spots centered around z_0, with the central focus gradually moving along the z-axis. As z_0 increases, the central focus moves away from the center and shifts gradually to the right. These spots closely approximate the expected intensity of a spherical light spot, and the corresponding Figs. 3(a)–(j) demonstrate that the intensity distribution remains approximately spherical throughout the entire translation range.

Figures 3(a)–(j) demonstrate that by altering the phase of the input field, the spherical light spots can move along the x-axis and z-axis. When the light spots need to move

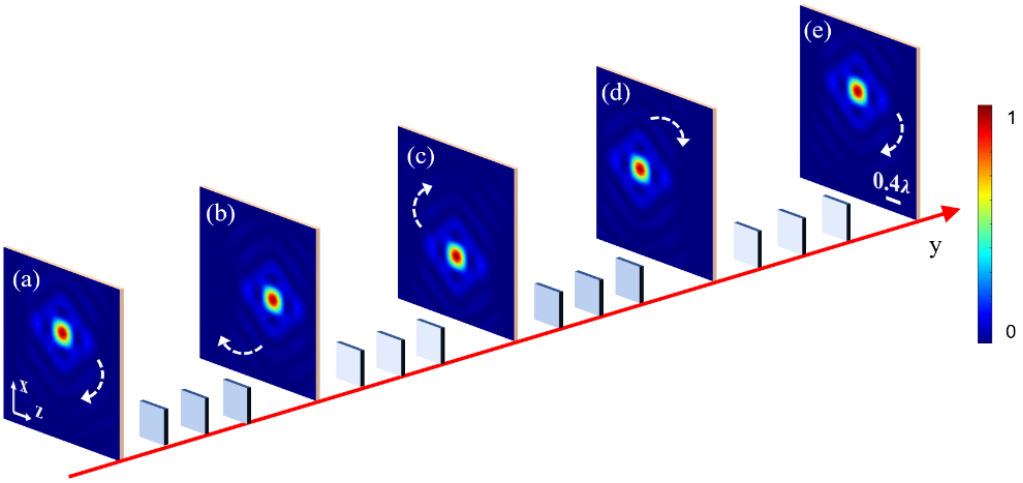

Fig. 4. Spherical focal spot movement along a circular path with radius $r = 0.5\lambda$ achieved via phase modulation. Subfigures (a)–(e) show spot position at coordinates $(0, 0.5\lambda)$, $(0.5\lambda, 0)$, $(0, -0.5\lambda)$, $(-0.5\lambda, 0)$, and $(0, 0.5\lambda)$ in the z-x plane.

along different paths, both parameters z_0 and x_0 can be adjusted simultaneously. Subfigures (k) and (l) demonstrate the distribution of a spherical spot in the focal area along the z-axis and along the x-axis of a 3D surface of equal intensity.

Figure 4 illustrates the movement of the spherical light spots near the focus along a circular path at $r = 0.5\lambda$. As shown, the spots in subfigures (a)–(e) appear at the coordinates (z, x) at $(0, 0.5\lambda)$, $(0.5\lambda, 0)$, $(0, -0.5\lambda)$, $(-0.5\lambda, 0)$, and $(0, 0.5\lambda)$, respectively. This also shows that by using the corresponding phase modulation, the spherical focal spot has been precisely transferred to the preconceived position.

To generate a transverse OV in space, we superimposed a phase factor $\exp(-il\varphi_{st})$. $l\varphi_{st}$ denotes the spatiotemporal spiral phase and $\varphi_{st} = \tan^{-1}(x/t)$. Take the first-order STOVs as an example, *i.e.*, when $l = 1$. By adjusting the phase, allowing the light spots to repeat n times within 2π radians. By dividing 2π into n segments, we obtain a discrete collection of light spots, as illustrated in Fig. 5 for $n = 10$, 20 and 30, respectively. In Fig. 5(a) ten spherical spots discretely distributed in three-dimensional space are shown. It shows the spiral vortex shape of light propagating forward in three-dimensional space, and this intensity distribution characteristic is highly consistent with the spatiotemporal optical vortex. These plots presented in the z-x plane are shown in Fig. 5(b).

Figure 6 depicts the square and circular ring formed when $n = 100$. Figures 6(a)–(c) show the movement of the spherical light spot near the focus along square paths defined by $a = 2$, 4 and 6 through phase modulation. As the selected value of n increases, the gaps between the light spots diminish. By selecting 100 spherical foci generated by the 4π tight focusing system and aligning them along a specified path to form a complete square, we can observe that placing all spots along the square path on the same plane results in a composite square of multiple spots. Additionally, the spots can be positioned at specified locations to create different shapes. To create spatially trans-

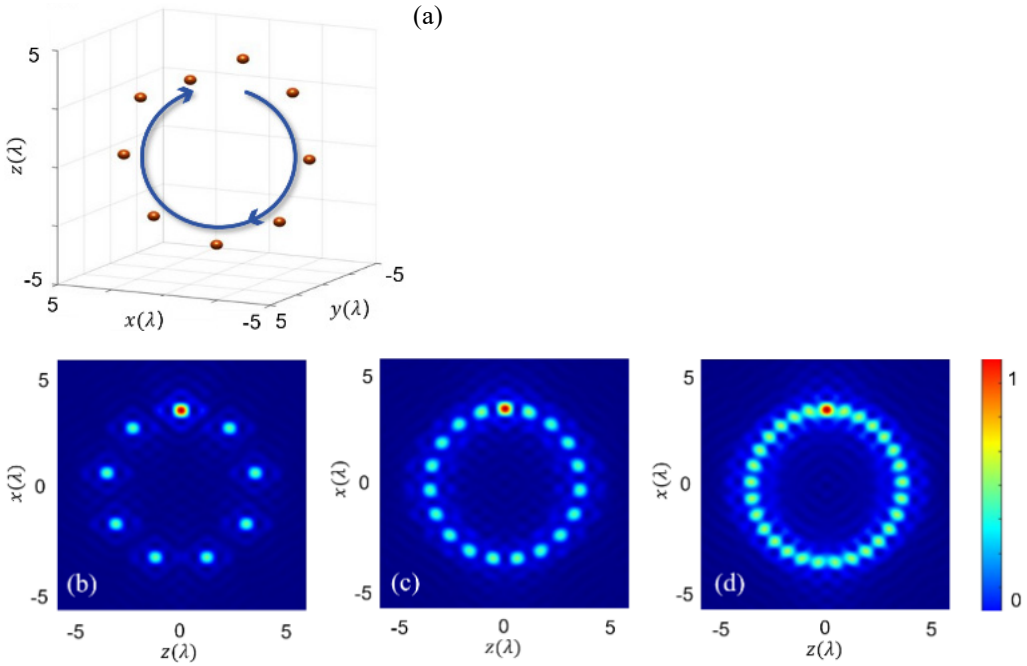

Fig. 5. Spherical focal spot movement along a circular path of $r = 3\lambda$, forming discretely distributed light spots in the *z*-*x* plane. (a) Ten spherical spots discretely distributed in 3D space. (b)–(d) Circles composed of 10, 20, and 30 discrete points in the *z*-*x* plane.

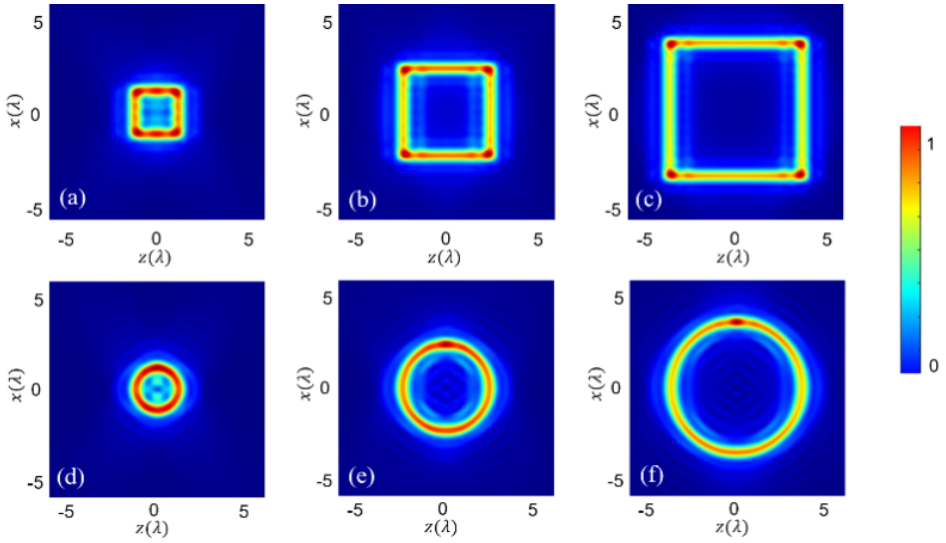

Fig. 6. Multiple spherical focal points generated by the 4π tight system forming distinct patterns in the *z*-*x* plane. (a)–(c) Square trajectories defined by parameters x_0 and z_0 (paths at $a = 2$, 4 and 6) via phase modulation. (d)–(f) Circular trajectories with radii $r = 1\lambda$, 2λ and 3λ achieved by jointly adjusting discretization and radius.

verse OVs, we defined a circular path with a radius of λ, 2λ, 3λ by varying the phase. When n is chosen to be sufficiently large, the light appears continuous, resulting in a smooth circular ring observed in the z-x plane. In reality, this manifests as transverse OVs in space. The hollow ring structure observed in the z-x plane, with zero intensity at its center, directly proves the existence of phase singularities, indicating that the electric field undergoes complete destructive interference at that point. Figures 6(d)–(f) show that by altering the phase, the spherical focal spots near the focus can traverse circular paths at $r = \lambda$, 2λ and 3λ. Thus, it can be observed that by adjusting the discretization and radius, an ideal synthetic circular light ring can be achieved, where a sufficient number of light spots results in a circle with no abrupt phase changes. It can also be adjusted to any shape, here two shapes, the square and the original shape, are used as examples.

As shown in Fig. 6(d), the circular ring formed by the light spots exhibits some scattered light in the center due to the small radius, as diffraction rings appear around the focus, preventing a completely hollow center. However, this also validates our approach: by altering the phase of the light spots, transverse OVs can exist in space, manifested as a circular ring in the z-x plane. As the radius of the circle increases, the hollow state of the ring becomes clearer.

To achieve a perfect ring structure, we enlarge the radius, allowing the focused light spots to form a seamless, ideal, and hollow ring in the z-x plane. As illustrated in Figs. 6(e) and (f), we modify the phase to move the spherical focal spots along circular paths at $r = 2\lambda$ and $r = 3\lambda$. The circular ring is composed of 100 spherical light spots, generated by a tight focusing radially polarized beam of 4π.

4. Conclusions

In summary, we theoretically demonstrate a novel method to generate spatially varying uniform STOVs by 4π tight focusing system. By independently designing the phase wavefronts of counter-propagating beams, we generate a uniform nano-scale spherical spots in the focal region. Then, treating spherical spots as spatial trajectory units and superimposing a time-dependent helical phase factor $\exp(-il\varphi_{st})$ allows for precise control over both the spatial position and movement trajectory of the light spots. This enables the generation of arbitrary dispersion patterns and trajectory manipulations in the spatio-temporal domain. When the temporal step is sufficiently small, *i.e.*, under high temporal resolution, smooth STOVs emerge. Through simultaneous modulation of temporal and spatial factor, STOVs with distinct radii r can be generated. This approach ultimately enables precise customization of STOVs in size, smoothness, and geometry, thereby offering substantial potential for advanced applications in optical communication systems, high-precision optical detection, and multi-particle manipulation using optical trapping technique.

Acknowledgement

Parts of this work were supported by the National Key R&D Program of China (2024YFF0507202 and 2021YFF0502900), National Natural Science Foundation of China (62305222/62375183/62127819/

T2421003/62435011), Shenzhen Key Laboratory of Photonics and Biophotonics (ZDSYS2021062309-2006020), and Shenzhen Science and Technology Program (JCYJ20220818100202005).

Declaration of competing interest
The authors declare that they have no known competing financial interests or personal relationships that could have appeared to influence the work reported in this paper.

Data availability
Data will be made available on request.

References

[1] Gao P., Prunsche B., Zhou L., Nienhaus K., Nienhaus G.U., *Background suppression in fluorescence nanoscopy with stimulated emission double depletion*, Nature Photonics **11**(3), 2017: 163-169. https://doi.org/10.1038/nphoton.2016.279

[2] Schmidt R., Wurm C.A., Jakobs S., Engelhardt J., Egner A., Hell S.W., *Spherical nanosized focal spot unravels the interior of cells*, Nature Methods **5**(6), 2008: 539-44. https://doi.org/10.1038/nmeth.1214

[3] Chen R., Zhou H., Moretti M., Wang X.D., Li J.D., *Orbital angular momentum waves: Generation, detection, and emerging applications*, IEEE Communications Surveys & Tutorials **22**(2), 2020: 840-868. https://doi.org/10.1109/COMST.2019.2952453

[4] Wang J., Yang J.Y., Fazal I.M., Ahmed N., Yan Y., Huang H., Ren Y.X., Yue Y., Dolinar S., Tur M., Willner A.E., *Terabit free-space data transmission employing orbital angular momentum multiplexing*, Nature Photonics **6**(7), 2012: 488-496. https://doi.org/10.1038/nphoton.2012.138

[5] Bozinovic N., Yue Y., Ren Y.X., Tur M., Kristensen P., Huang H., Willner A.E., Ramachandran S., *Terabit-scale orbital angular momentum mode division multiplexing in fibers*, Science **340**(6140), 2013: 1545-1548. https://doi.org/10.1126/science.1237861

[6] Willner A.E., Pang K., Song H., Zou K.H., Zhou H.B., *Orbital angular momentum of light for communications*, Applied Physics Reviews **8**(4), 2021: 041312. https://doi.org/10.1063/5.0054885

[7] Wang X.L., Cai X.D., Su Z.E., Chen M.C., D. Wu, L. Li, Liu N.L., Lu C.Y., Pan J.W., *Quantum teleportation of multiple degrees of freedom of a single photon*, Nature **518**(7540), 2015: 516-519. https://doi.org/10.1038/nature14246

[8] Wang X.Y., Zhao S.H., C. Dong, Zhu Z.D., Gu W.Y., *Orbital angular momentum-encoded measurement device independent quantum key distribution under atmospheric turbulence*, Quantum Information Processing **18**(10), 2019: 304. https://doi.org/10.1007/s11128-019-2424-1

[9] Mirhosseini M., Magaña-Loaiza O.S., O'Sullivan M.N., Rodenburg B., Malik M., Lavery M.P.J., Padgett M.J., Gauthier D.J., Boyd R.W., *High-dimensional quantum cryptography with twisted light*, New Journal of Physics **17**, 2015: 033033. https://doi.org/10.1088/1367-2630/17/3/033033

[10] Boyd R.W., Rodenburg B., Mirhosseini M., Barnett S.M., *Influence of atmospheric turbulence on the propagation of quantum states of light using plane-wave encoding*, Optics Express **19**(19), 2011: 18310-18317. https://doi.org/10.1364/OE.19.018310

[11] Grier D.G., *A revolution in optical manipulation*, Nature **424**(6950), 2003: 810-816. https://doi.org/10.1038/nature01935

[12] Padgett M., Bowman R., *Tweezers with a twist*, Nature Photonics **5**(6), 2011: 343-348. https://doi.org/10.1038/nphoton.2011.81

[13] Nobre-Pereira J., De Angelis V.S., Ambrosio L.A., Zamboni-Rached M., *Exact analytical solutions for micrometer structured vortex beams with applications to optical tweezers*, Optics and Laser Technology **171**, 2024: 110374. https://doi.org/10.1016/j.optlastec.2023.110374

[14] Huang S.L., Li Z.W., Li J.W., Zhang N., Lu X., Dorfman K., Liu J., Yao J.P., *Spatiotemporal vortex strings*, Science Advances **10**(19), 2024: eadn6206. https://doi.org/10.1126/sciadv.adn6206

[15] BLIOKH K.Y., NORI F., *Spatiotemporal vortex beams and angular momentum*, Physical Review A **86**(3), 2012: 033824. https://doi.org/10.1103/PhysRevA.86.033824
[16] BLIOKH K.Y., NORI F., *Transverse and longitudinal angular momenta of light*, Physics Reports **592**, 2015: 1-38. https://doi.org/10.1016/j.physrep.2015.06.003
[17] SUKHORUKOV A.P., YANGIROVA V.V., *Spatio-temporal vortices: properties, generation and recording*, Proceedings of the SPIE, Vol. 5949, Nonlinear Optics Applications, 2005: 594906. https://doi.org/10.1117/12.623906
[18] JHAJJ N., LARKIN I., ROSENTHAL E.W., ZAHEDPOUR S., WAHLSTRAND J.K., MILCHBERG H.M., *Spatio-temporal optical vortices*, Physical Review X **6**, 2016: 031037. https://doi.org/10.1103/PhysRevX.6.031037
[19] CHONG A., WAN C., CHEN J., ZHAN Q., *Generation of spatiotemporal optical vortices with controllable transverse orbital angular momentum*, Nature Photonics **14**(6), 2020: 350-354. https://doi.org/10.1038/s41566-020-0587-z
[20] HANCOCK S.W., ZAHEDPOUR S., GOFFIN A., MILCHBERG H.M., *Free-space propagation of spatiotemporal optical vortices*, Optica **6**(12), 2019: 1547-1553. https://doi.org/10.1364/OPTICA.6.001547
[21] HUANG S.L., WANG P., SHEN X., LIU J., *Properties of the generation and propagation of spatiotemporal optical vortices*, Optics Express **29**(17), 2021: 26995-27003. https://doi.org/10.1364/OE.434845
[22] HUANG J.Y., ZHANG J.H., ZHU T.F., RUAN Z.C., *Spatiotemporal differentiators generating optical vortices with transverse orbital angular momentum and detecting sharp change of pulse envelope*, Laser and Photonics Reviews **16**(5), 2022: 2100357. https://doi.org/10.1002/lpor.202100357
[23] YOUNGWORTH K.S., BROWN T.G., *Focusing of high numerical aperture cylindrical-vector beams*, Optics Express **7**(2), 2000: 77-87. https://doi.org/10.1364/OE.7.000077
[24] TIAN B., PU J.X., *Tight focusing of a double-ring-shaped, azimuthally polarized beam*, Optics Letters **36**(11), 2011: 2014-2016. https://doi.org/10.1364/OL.36.002014

Received September 19, 2025
in revised form October 14, 2025